Mechanistic-mathematical modeling of intracranial pressure (ICP) profiles over a single heart cycle. The fundament of the ICP curve form

Domogo, Andrei A.; Reinstrup, Peter; Ottesen, Johnny T.

Published in:
Journal of Theoretical Biology

DOI:
10.1016/j.jtbi.2023.111451

Publication date:
2023

Document Version
Publisher's PDF, also known as Version of record

Citation for published version (APA):
Domogo, A. A., Reinstrup, P., & Ottesen, J. T. (2023). Mechanistic-mathematical modeling of intracranial pressure (ICP) profiles over a single heart cycle. The fundament of the ICP curve form. *Journal of Theoretical Biology*, *564*, [111451]. https://doi.org/10.1016/j.jtbi.2023.111451

Journal of Theoretical Biology 564 (2023) 111451

Contents lists available at ScienceDirect

Journal of Theoretical Biology

journal homepage: www.elsevier.com/locate/yjtbi

Mechanistic-mathematical modeling of intracranial pressure (ICP) profiles over a single heart cycle. The fundament of the ICP curve form

Andrei A. Domogo [a,d], Peter Reinstrup [b], Johnny T. Ottesen [c,d,*]

[a] Department of Mathematics and Computer Science, University of the Philippines Baguio, Baguio City 2600, Philippines
[b] Intensive and Perioperative Care, Skåne University Hospital, Lund, Sweden
[c] Center for Mathematical Modeling - Human Health and Disease (COMMAND), Roskilde University, 4000 Roskilde, Denmark
[d] IMFUFA, Department of Science and Environment, Roskilde University, 4000 Roskilde, Denmark

ARTICLE INFO

Keywords:
Mathematical modeling
Patient-specific
Parameter estimation
Intracranial hydrodynamics
ICP curve morphology

ABSTRACT

The intracranial pressure (ICP) curve with its different peaks has been comprehensively studied, but the exact physiological mechanisms behind its morphology has not been revealed. If the pathophysiology behind deviations from the normal ICP curve form could be identified, it could be vital information to diagnose and treat each single patient. A mathematical model of the hydrodynamics in the intracranial cavity over single heart cycles was developed. A Windkessel model approach was generalized but the unsteady Bernoulli equation was utilized for blood flow and CSF flow. This is a modification of earlier models using the extended and simplified classical Windkessel analogies to a model that is based on mechanisms rooted in the laws of physics. The improved model was calibrated with patient data for cerebral arterial inflow, venous outflow, cerebrospinal fluid (CSF), and ICP over one heart cycle from 10 neuro-intensive care unit patients. A priori model parameter values were obtained by considering patient data and values taken from earlier studies. These values were used as an initial guess for an iterated constrained-ODE (ordinary differential equation) optimization problem with cerebral arterial inflow data as input into the system of ODEs. The optimization routine found patient-specific model parameter values that produced model ICP curves that showed excellent agreement with clinical measurements while model venous and CSF flow were within a physiologically acceptable range. The improved model and the automated optimization routine gave better model calibration results compared to previous studies. Moreover, patient-specific values of physiologically important parameters like intracranial compliance, arterial and venous elastance, and venous outflow resistance were determined. The model was used to simulate intracranial hydrodynamics and to explain the underlying mechanisms of the ICP curve morphology. Sensitivity analysis showed that the order of the three main peaks of the ICP curve was affected by a decrease in arterial elastance, a large increase in resistance to arteriovenous flow, an increase in venous elastance, or a decrease in resistance to CSF flow in the foramen magnum; and the frequency of oscillations were notably affected by intracranial elastance. In particular, certain pathological peak patterns were caused by these changes in physiological parameters. To the best of our knowledge, there are no other mechanism-based models associating the pathological peak patterns to variation of the physiological parameters.

1. Introduction

Continuous monitoring of ICP in humans was introduced by Guillaume and Janny (1951) and the progress into a clinical application was done by Lundberg (1960). Since then, it has been an important monitoring procedure in the treatment of hydrocephalus (Eide and Brean, 2006; Kim et al., 2009), traumatic brain injury (Hu et al., 2010; Daouk et al., 2016), subarachnoid hemorrhage (Balédent et al., 2018), and other brain diseases. The physiology behind the morphology of the ICP curve is, however, not fully understood (Unnerbäck et al., 2018, 2020). Several studies involving ICP pulse amplitude have been done in specific clinical settings but the causes underlying ICP curve morphology are still uncertain (Balédent et al., 2018) even though intracranial compliance is involved. Intracranial compliance is a vague concept and with an incompressible brain tissue being the sum (maybe non-algebraic) of three: the compliance of the venous pool, the compliance

* Corresponding author at: Center for Mathematical Modeling - Human Health and Disease (COMMAND), Roskilde University, 4000 Roskilde, Denmark.
E-mail addresses: aadomogo1@up.edu.ph (A.A. Domogo), peter.reinstrup@med.lu.se (P. Reinstrup), johnny@ruc.dk (J.T. Ottesen).

https://doi.org/10.1016/j.jtbi.2023.111451
Received 20 October 2021; Received in revised form 31 December 2022; Accepted 28 February 2023
Available online 11 March 2023

of the cerebrospinal fluid (CSF) pool, and the compliance of the arterial pool (Czosnyka and Citerio, 2012).

Obtaining knowledge on the parameters constituting the intracranial compliance is challenging, both in practical and ethical aspects (Unnerbäck et al., 2020). In humans, arterial inflow and venous outflow in the cranium as well as CSF flow over the foramen magnum can be measured through cine phase contrast MRI (Balédent et al., 2001; Alperin et al., 2005; Stoquart-ElSankari et al., 2009) and ICP measured invasively with high time resolution (Unnerbäck et al., 2020). Recently, these parameters were measured simultaneous in 10 neuro-intensive care patients (Unnerbäck et al., 2018). It was conjectured that such approach would lead to an increase in knowledge of the underlying pathophysiology in brain diseases (Balédent et al., 2018).

Through a mathematical model, we can take into account different features of intracranial dynamics simultaneously and access information that were otherwise challenging to obtain experimentally [Ottesen (2011)]. An original mathematical model of the human long-term changes in intracranial hydrodynamics was suggested by Ursino (1988). Different properties of the intracranial system were also explored using mathematical models [Marmarou et al. (1978); Ursino and Lodi (1997); Stevens (2000); Linninger et al. (2005, 2009)]. In particular, Marmarou et al. (1978) used a mathematical model based on a Windkessel analogy to improve the analysis of intracranial dynamic properties, Czosnyka et al. (1990) designed a computer system for the cerebrospinal compensatory model identification, Eklund et al. (2007) presented a mathematical model for determining intracranial dynamic properties with specific focus on CSF outflow resistance, and Støverud et al. (2013) examined CSF flow using the Bernoulli equation and Navier–Stokes equation. Recently, a mathematical model based on known physiological properties of the intracranial compartment, looking at changes over a single heartbeat, was presented [Unnerbäck et al. (2020)]. The model was able to mimic ICP measured in vivo based on arterial intracranial inflow and the compensatory mechanisms taking place in the intracranial cavity.

The goal of the present study was to develop an improved mechanistic-mathematical model of cerebral blood flow (CBF) and then to calibrate it with patient-specific data using an optimization routine. After which, variation of the model parameter values helped us identify the mechanisms intrinsic in changes in the ICP curve morphology. In order to achieve our goal, we asked the following questions. What compartments and state variables were needed to be considered? What formulation of CBF and CSF were suitable? What pressure–volume relation should be utilized? Could ICP data be used to estimate reliable model parameters? Would the established optimal parameters give rise to realistic intracranial dynamics? Could intracranial compliance be measured directly using estimated model parameters and could the model simulation be an alternative to measure intracranial compliance by response to injection/removal of CSF? Finally, which parameters governed the ICP curve morphology and what insights it can provide?

2. Methods

2.1. Data

Data for arterial inflow, venous outflow, CSF flow, and ICP from 10 neuro-intensive care unit patients at Skåne University Hospital, Lund were used. These data have been previously published in Unnerbäck et al. (2020) but new analyses are made here, which resulted to new findings. The average age of the patients was 49 ± 11 years old. The main diagnoses of the patients were 6 with traumatic brain injury, 2 with subarachnoid haemorrhage, 1 with meningitis, and 1 with obstructive hydrocephalus. Cerebral arterial inflow, venous outflow, and CSF flow were obtained through flow sensitive slices just under the skullbase with cine-phase contrast MRI while ICP was measured with an 8-F tunneled intraventricular catheter placed through a cranial burr hole. For a full and detailed description of the method see Unnerbäck et al. (2020).

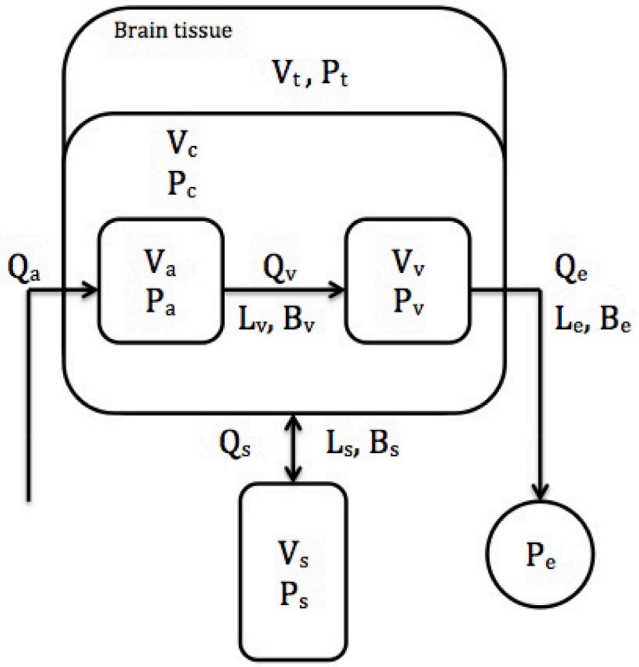

Fig. 1. Block diagram of cerebral blood and CSF flow. The letters in the diagram stand for volume (V), pressure (P), flow (Q), inertia (L), and Bernoulli/resistance parameter (B). The subscripts represent arteries (a), veins (v), intracranial (c), spine (s), tissue (t), and exit (e). CBF is through the arterial and venous compartments and CSF flows back and forth from the intracranial cavity to the spinal canal through the foramen magnum.

2.2. Model formulation

The model formulation started with a compartmental visualization of CBF and CSF flow given in Fig. 1. This is a novel way of looking at the compartments in the intracranial cavity as proposed by Unnerbäck et al. (2020). We extend this model by improving the simplified classical Windkessel analogies to a model that uses the unsteady Bernoulli equation for flow and a mono-exponential pressure–volume relation for nonnegative transmural pressure.

The idea was to look at a compartment containing compartments. Instead of considering a separate compartment for the intracranial CSF, we looked at a larger compartment. We denoted it as the intracranial compartment, which contains the intracranial arterial, venous, and CSF compartments. This simplified the inclusion of the intracranial CSF compartment in the model without having to deal with its different borders. This formulation made it possible to avoid direct determination of the compliance of the intracranial CSF compartment and the pressure outside this compartment. Note that the compliance of the intracranial CSF compartment is a function of the compliances of the arterial, venous, and brain tissue compartments. Furthermore, the pressure in the intracranial compartment is the ICP and the compliance of this compartment can be thought of as the intracranial compliance. To separate the brain tissue compartment is natural because it was presumed not to take in or give off fluid to the other compartments during a heartbeat.

In the following, we build the model equations based on known physiological relations. The letters in the equations stand for volume (V), pressure (P), flow (Q), inertance (L), and Bernoulli parameter (B). The subscripts stand for arteries (a), veins (v), intracranial (c), spine (s), tissue (t), exit (e), and unstressed (u).

Change in volumes. A conservation law was used to describe the rate of change of volume in a compartment. This states that the time derivative of volume in a compartment at time t is equal to the

difference between the flow in and flow out of the compartment. In symbols, $\dot{V}(t) = Q_{in}(t) - Q_{out}(t)$, where dot on the top of a symbol denote the time derivative of the corresponding quantity. If we let the stressed volume be given by ΔV then $\Delta V(t) := V(t) - V_u(t)$, where V_u denotes the unstressed volume. This implies that $\Delta\dot{V}(t) = \dot{V}(t) = Q_{in}(t) - Q_{out}(t)$, assuming that $V_u(t)$ is constant over a single heart beat. Thus,

$$\Delta\dot{V}_a(t) = Q_a(t) - Q_v(t) \tag{1}$$

$$\Delta\dot{V}_v(t) = Q_v(t) - Q_e(t) \tag{2}$$

$$\Delta\dot{V}_c(t) = Q_a(t) - Q_s(t) - Q_e(t) \tag{3}$$

$$\Delta\dot{V}_s(t) = Q_s(t) \tag{4}$$

Arteriovenous flow, CSF flow, and venous outflow. The arteriovenous flow, CSF flow, and flow out of cranium was assumed to be governed by the unsteady Bernoulli equation (Grimes et al., 1995; Domogo and Ottesen, 2021).

$$\dot{Q}_v(t) = \frac{1}{L_v}[P_a(t) - P_v(t) - B_v|Q_v(t)|Q_v(t)] \tag{5}$$

$$\dot{Q}_s(t) = \frac{1}{L_s}[P_c(t) - P_s(t) - B_s|Q_s(t)|Q_s(t)] \tag{6}$$

$$\dot{Q}_e(t) = \frac{1}{L_e}[P_v(t) - P_e(t) - B_e|Q_e(t)|Q_e(t)] \tag{7}$$

Pressure–volume relations. The relation between pressure and volume in a compartment was based on blood vessel compliance. This states that the volume in a compartment is an increasing function of pressure. In terms of elastance, the reciprocal of compliance, this says that the difference between pressure inside and outside of the compartment is an increasing function of volume. In simplified cases, as in the Windkessel model, a linear relation is assumed. However, we used the more general monoexponential relationship between cerebral arterial blood volume and cerebral arterial transmural pressure (Bergel, 1961; Hayashi et al., 1980) and similarly with CSF volume and ICP (Marmarou et al., 1978; Avezaat et al., 1979). This assumption can also be made for the relationship between cerebral venous blood volume and cerebral venous transmural pressure (Ursino, 1988). Due to the incidence of venous collapse, we only assumed the monoexponential relationship for nonnegative transmural pressure. For negative transmural pressure, we chose a function that can mimic the behavior of the pressure–volume relation in collapsible tubes as given in Rideout (1991).

$$P_c(t) = P_{c0}(e^{K_c\Delta V_c(t)} - 1) + P_t \tag{8}$$

$$P_a(t) = P_{a0}(e^{K_a\Delta V_a(t)} - 1) + P_c \tag{9}$$

$$P_v(t) = \begin{cases} P_{v0}(e^{K_v\Delta V_v(t)} - 1) + P_c & \text{if } \Delta V_v(t) \geq 0 \\ (P_{v0}K_vV_{vu})(\frac{\Delta V_v(t)}{\Delta V_v(t)+V_{vu}}) + P_c & \text{if } \Delta V_v(t) < 0 \end{cases} \tag{10}$$

$$P_s(t) = P_{s0}(e^{K_s\Delta V_s(t)} - 1) + P_{s,out} \tag{11}$$

In the equations given in (8)–(11), we see that zero transmural pressure corresponds to stressed volume being zero and the venous relation fulfill a smoothness demand at $\Delta V_v = 0$. We also emphasize, linearizing the mono-exponential expressions result in the usual Windkessel approximation.

In summary, the model was described by 7 ODEs given by Eqs. (1)–(7), 4 algebraic equations given by Eqs. (8)–(11), and 18 model parameters given by the elastance coefficients K_c, K_a, K_v, K_s, P_{c0}, P_{a0}, P_{v0}, and P_{s0}, pressure parameters P_e, P_t, and $P_{s,out}$, inertances L_v, L_s, and L_e, Bernoulli parameters B_v, B_s, and B_e, and unstressed volume in the veins V_{vu}. In the following, we do not include in the notation the dependence of the equations on time for a neater presentation.

Brain tissue movement. The skull is rigid, consequently, its volume is constant. That is, $V_c + V_t = V_{skull}$ is constant, by the Monro-Kellie doctrine $\dot{V}_c + \dot{V}_t = \Delta\dot{V}_c + \Delta\dot{V}_t = 0$. Using this conservation formula, the slight compression of the brain tissue follows $\Delta\dot{V}_t = -\Delta\dot{V}_c$.

Change in CSF volume in the cranium. Note that CSF production is slow and (relatively) steady at about 0.35 ml/min (McArdle et al., 2006). Furthermore, we assumed that CSF production was equal to its absorption and elimination. Thus, the total volume of CSF, denoted by V_{csf}, was constant over the period of one heart beat. Hence, $V_{csf(intracranial)} + V_s = V_{csf}$ and $\dot{V}_{csf(intracranial)} + \dot{V}_s = \Delta\dot{V}_{csf(intracranial)} + \Delta\dot{V}_s = 0$. How the intracranial CSF changes through a heart cycle could then be observed using $\Delta\dot{V}_{csf(intracranial)} = -\Delta\dot{V}_s$.

Compliance of the compartments. The compliance of the compartments could be obtained through their respective pressure–volume relationship. For the arterial compartment, the pressure–volume relation is given by Eq. (9). Expressing this equation as volume in terms of pressure,

$$V_a - V_{au} = \frac{1}{K_a}\ln(P_a - P_c + P_{a0}) - \frac{1}{K_a}\ln P_{a0}. \tag{12}$$

Hence, the compliance of the arterial compartment, C_a, is given by

$$C_a = \frac{dV_a}{d(P_a - P_c)} = \frac{1}{K_a(P_a - P_c + P_{a0})} = \frac{1}{K_aP_{a0}}e^{-K_a\Delta V_a} \tag{13}$$

Similarly, the compliance of the other compartments are

$$C_c = \frac{dV_c}{d(P_c - P_t)} = \frac{1}{K_c(P_c - P_t + P_{c0})} = \frac{1}{K_cP_{c0}}e^{-K_c\Delta V_c}, \tag{14}$$

$$C_s = \frac{dV_s}{d(P_s - P_{s,out})} = \frac{1}{K_s(P_s - P_{s,out} + P_{s0})} = \frac{1}{K_sP_{s0}}e^{-K_s\Delta V_s}, \tag{15}$$

and

$$C_v = \frac{dV_v}{d(P_v - P_c)} = \begin{cases} \frac{1}{K_v(P_v - P_c + P_{v0})} = \frac{1}{K_vP_{v0}}e^{-K_v\Delta V_v} & \text{if } \Delta V_v \geq 0 \\ \frac{P_{v0}K_vV_{vu}^2}{(P_v - P_c - P_{v0}K_vV_{vu})^2} = \frac{(\Delta V_v + V_{vu})^2}{P_{v0}K_vV_{vu}^2} & \text{if } \Delta V_v < 0 \end{cases}. \tag{16}$$

Notice the elastances become linearly increasing function of the transmural pressure or an exponential function of stressed volume, except in the case of venous collapse. That is,

$$e_a = K_a(P_a - P_c) + K_aP_{a0} = K_aP_{a0}e^{K_a\Delta V_a}, \tag{17}$$

$$e_c = K_c(P_c - P_t) + K_cP_{c0} = K_cP_{c0}e^{K_c\Delta V_c}, \tag{18}$$

$$e_s = K_s(P_s - P_{s,out}) + K_sP_{s0} = K_sP_{s0}e^{K_s\Delta V_s}, \tag{19}$$

$$e_v = \begin{cases} K_v(P_v - P_c) + K_vP_{v0} = K_vP_{v0}e^{K_v\Delta V_v} & \text{if } \Delta V_v \geq 0 \\ \frac{1}{P_{v0}K_vV_{vu}^2}(P_v - P_c - P_{v0}K_vV_{vu})^2 = \frac{P_{v0}K_vV_{vu}^2}{(\Delta V_v + V_{vu})^2} & \text{if } \Delta V_v < 0 \end{cases}. \tag{20}$$

From the elastance expressions, we may term the $K_i's$ as the stressed elastance parameters and $(P_{i0}K_i)'s$ the unstressed elastance parameters.

2.3. Parameter estimation

The objective of this section is to find parameter values that will give intracranial pressure curve that conforms with given data. Additionally, we wanted the system to be in a periodic state, which is the model equivalent of the stable condition of the patients (i.e. Homeostatic resting conditions) when the data was collected. The parameter estimation process started with (1) an a priori parameter estimation followed by (2) an iterated optimization. Note that arterial inflow data were used as input to the model, ICP data were used in the optimization problem, while venous outflow and CSF flow in the foramen magnum were used as control values for comparison with model output.

In the a priori estimation, available data and related literature were used to calculate parameter values for the model. For the iterated optimization, we used the a priori parameter values as initial guess for a minimization problem. The minimization problem was solved numerically in Matlab using the *fmincon* function. The objective cost of this minimization problem is given by

$$\begin{aligned}\text{Obj. Cost} \quad = \quad & \sum_{i=0}^{N-1}\left\{\frac{P_c(t_i) - P_c^*(t_i)}{P_c^*(t_i)}\right\}^2 + w\sum_{i\in J}\left\{\frac{P_c(t_i) - P_c^*(t_i)}{P_c^*(t_i)}\right\}^2 \\ & + \gamma_1\sum_{i\in K}\left\{\Delta V_s(t_i)\right\}^2 + \gamma_2\sum_{i=a,v,c,s}\left\{\Delta V_i(T) - \Delta V_i(0)\right\}^2.\end{aligned}$$

The first term of the objective cost function is the sum of squares of the relative error between intracranial pressure from model simulation and data. $P_c(t_i)$ is the intracranial pressure from model simulation while $P_c^*(t_i)$ is the intracranial pressure from data. The $t_i's$ are N equally spaced time instances from 0 to T (duration of a heart cycle where data exist). The second term was added to give more weight, w, to the peaks and valleys of the intracranial pressure data whose indices are contained in set J. The third and fourth terms are penalty terms, where γ_1 and γ_2 are sufficiently large values. Since the spinal compartment was assumed not be compressed, the third term was added so that the optimization avoids parameter values that give negative values for ΔV_s. In this term, K is the index set containing all $i \in \{0, 1, \ldots, N-1\}$ such that $\Delta V_s(t_i) < 0$. The fourth term was added so that the optimization favors parameter values that give rise to a periodic state. We note that if the stressed volumes are periodic then the pressures and flows become periodic.

2.3.1. A priori parameter estimation

Elastance parameters

For the elastance parameters, we took $K_a = 3.68$ and $K_v = 0.31$ per ml from Ursino (1988). We assumed that $K_c = 3$ and $K_s = 2$ per ml since the intracranial compartment is not a very compliant compartment and the spinal compartment is a little more compliant. The elastance of cerebral arteries is 12.66 mmHg/ml (Ellwein et al., 2008) and the cerebral veins is 0.43 mmHg/ml (Olufsen et al., 2005). Using Eqs. (17) and (20) and assuming zero transmural pressure, we have that $P_{a0} = e_a/K_a$ and $P_{v0} = e_v/K_v$. In this case, $P_{a0} = 3.44$ mmHg and $P_{v0} = 1.38$ mmHg. We assumed $P_{c0} = 10$ mmHg and $P_{s0} = 5$ mmHg since the craniospinal compartment is not very compliant.

Pressure Parameters

In Eq. (8) we see that $P_c = P_t$ when the stressed volume in the intracranial compartment is zero. We used this to estimate initial value of P_t as the minimum ICP value from patient data. We assumed that the initial outside pressure in the spinal compartment, $P_{s,out}$, is equal to P_t. The initial external venous pressure $P_e = 4.0$ mmHg was taken from Ursino (1988).

Inertance Parameters

The a priori estimate for $L_s = 0.1$ mmHg s^2/ml and $L_e = 0.14$ mmHg s^2/ml were taken from Unnerbäck et al. (2020). We assumed that $L_v = 0.001$ mmHg s^2/ml, which is a relatively smaller value because inertia in smaller blood vessels with low pressure gradients is less dominant in comparison to their resistance (Westerhof et al., 2005).

Bernoulli Parameters

In Unnerbäck et al. (2020), the formulation for change in flow between two compartments i and j is given by $\dot{Q} = \frac{1}{L}(P_i - P_j - RQ)$, where R is the classical resistance to flow. To agree with the Bernoulli formulation, R becomes flow dependent, that is, $R = B|Q|$. We used this idea to obtain an a priori estimate for the Bernoulli parameters B_s, B_e, and B_v. We have data for Q_s and Q_e and we know $R_s = 0.6$, $R_v = 12.54$, and $R_e = 0.54$ (Unnerbäck et al., 2020). From here, we take $B_s = R_s/|Q_s|$, $B_e = R_e/|Q_e|$, and $B_v = R_v/|Q_v|$, where $|Q_v|$ was approximated by Q_a from data. We used the maximum data value of Q_s, Q_e, and Q_a as the single value for the flows to get the a priori Bernoulli parameters.

Unstressed Volume Parameters

Blood volume in the intracranial cavity is 60–80 ml (Unnerbäck et al., 2018), of which, 15 ml is in the arteries (Hua et al., 2019). This gives 45 to 65 ml venous blood volume, of which, 80% is unstressed (Ellwein et al., 2008). Using this, we took $V_{vu} = 40$ ml as a priori value.

Initial Values

The initial values for the system of ODEs were given as follows. The initial values for the stressed volumes $\Delta V_a(0)$, $\Delta V_v(0)$, $\Delta V_c(0)$, and $\Delta V_s(0)$ were all set to zero corresponding to a steady state. The initial values for the flows $Q_s(0)$ and $Q_e(0)$ were taken from initial CSF flow data and initial venous outflow data, respectively, while $Q_v(0)$ was approximated by initial arterial flow data.

The a priori parameter values for the patients were calculated using the above formulas or values. They were used as an initial guess in the optimization process. However, the calculated optimal parameters for some patients were utilized as a priori parameters for other patients when they led to better model fit.

2.3.2. Optimization

The a priori parameters were used as initial guess for an iterated optimization. Here, we optimized all model parameters together with initial conditions except for L_v, V_{vu}, $Q_s(0)$, and $Q_e(0)$. Post sensitivity analysis showed that L_v and V_{vu} were not sensitive while $Q_s(0)$ and $Q_e(0)$ were fixed values from data. Notice the objective cost is a function of the parameter values and the change in stressed volume and flow output of the model. The state variables appearing in the objective cost are the stressed volumes but they are part of a system of ODEs. Hence, dependence on the other model output (flow state variables) is indirect. Now, if $X(par)$ is the change in stressed volume and flow output given the input parameters par, we have that

$$\text{Objective Cost} = f(par, X(par)).$$

Our goal was to minimize the objective cost in a given physiologically accepted region. We note that the initial guess to the minimization problem was the approximated a priori parameter values. These values may be away from the optimal values in different magnitude. We assumed that moving 50% above and below the initial parameters were suitable boundary values except for the initial stressed volumes. We assumed that $\Delta V_a(0) \in [0, 1.5]$, $\Delta V_v(0) \in [-1, 1]$, $\Delta V_c(0) \in [0, 1]$, and $\Delta V_s(0) \in [0, 1]$. $\Delta V_a(0)$, $\Delta V_c(0)$, and $\Delta V_s(0)$ are nonnegative because their respective compartments are not compressed with $\Delta V_c(0)$ and $\Delta V_s(0)$ having a lesser upper bound since these compartments are not so compliant. On the other hand, $\Delta V_v(0)$ is from $[-1, 1]$ to incorporate possible compression. In addition, the bounds were not large because the magnitude of the input arterial flow does not presumably make the initial stressed volume values go beyond the given bounds.

The Matlab functions $fmincon$ and $ODE15s$ were used to solve for the minimizer of f and system of ODEs, respectively. Since the minimization scheme was local in nature, we explored other minimizers about a neighborhood of a determined minimizer through the following iterative scheme adopted from Domogo and Ottesen (2021). We used the optimal parameters as initial guess for the next iterate of the minimization problem.

Initialization:
$init\_par$ = a priori parameters
$obj\_cost\_old = \infty$
$opt\_par = arg\_min$ of f, where $par \in [LB, UB]$
$obj\_cost = f(opt\_par, X(opt\_par))$
while $|obj\_cost - obj\_cost\_old|/obj\_cost < tol$ do:
  $obj\_cost\_old = obj\_cost$
  $init\_par = opt\_par$
  $opt\_par = arg\_min$ of f, where $par \in [LB, UB]$
  $obj\_cost = f(opt\_par, X(opt\_par))$

Furthermore, once the iterative scheme terminated, we used the optimal parameters to get a numerical solution to the system of ODEs for one period. We then used the terminal values of the state variables to replace their initial values and ran the iterative scheme again. We performed this perturbation a finite number of times or until the objective cost did vary less than a predefined tolerance. This additional perturbation helped the minimization process in looking for a periodic state, which is in accordance to the homeostatic state of the patients when the data was collected.

In the Matlab function $fmincon$, we used the default Interior Point Algorithm. This option looked for minimizers through a sequence of approximate minimization problems involving barrier functions. The approximate minimization problems were then solved by searching in

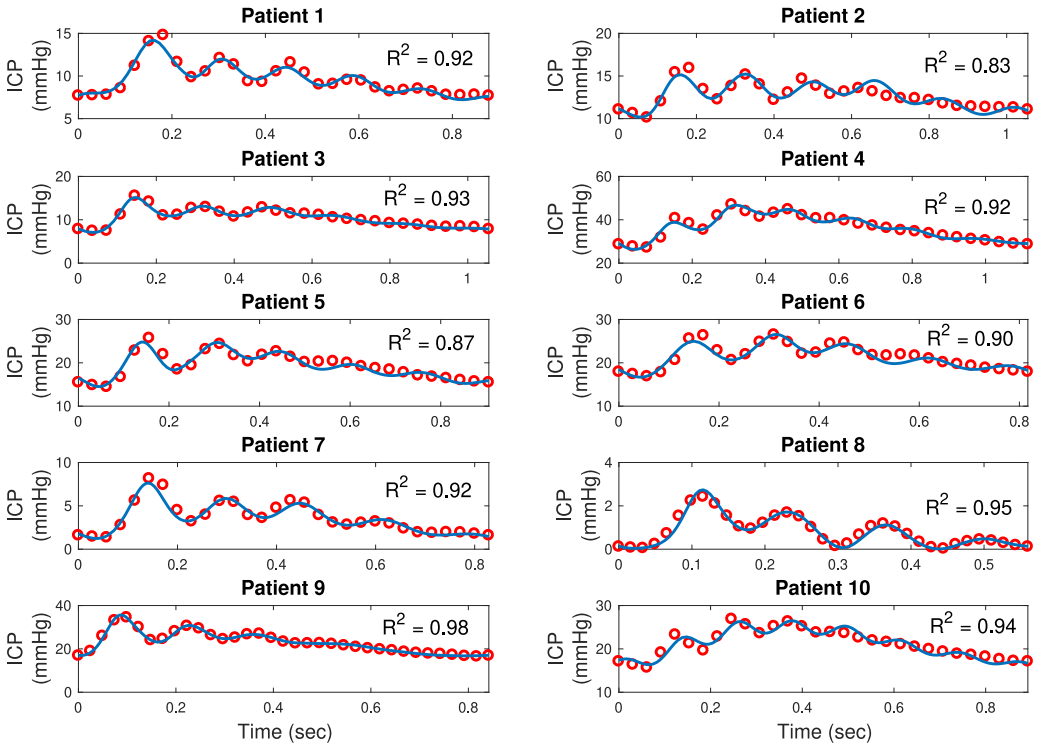

Fig. 2. The ICP curves for 10 patients. The blue lines are the ICP curves from the model and the red circles are data.

the direction of a Newton step in each iteration. If the Newton step failed, the function searched using a Conjugate Gradient step in a trust region (The Mathworks Inc., 2021). The codes for the optimization and system of ODEs are given in Supplementary F.

2.4. Model modification for ICP response

The effect of addition or leak of fluid in the intracranial compartment, V_c, can be simulated. To do this, we modified Eq. (3) by adding a flow term, Q_l, representing an addition or a leak. This resulted to Eq. (21).

$$\Delta\dot{V}_c = Q_a - Q_s - Q_e + Q_l \tag{21}$$

If Q_l is positive then it represents an addition of volume into the intracranial compartment. Correspondingly, a negative Q_l represents removal of volume out of the intracranial compartment. The ICP response to an addition/withdrawal of CSF from the intracranial compartment can be investigated by letting $Q_l \neq 0$ for a fixed time and then observing the changes in ICP at succeeding cycles.

3. Results

3.1. Model fit, optimal parameter values, and simulations

The simulated model curves showed that the model was able to capture the dynamics of cerebral blood flow and intracranial pressure. Through optimization, the model could be calibrated well to ICP data while also displaying venous outflow and CSF flow over the foramen magnum that were within acceptable physiological range.

Fig. 2 displays the calculated ICP curves from the calibrated model and ICP data for all patients. Here, we observed that the model was able to capture the individual ICP behavior from data as they can be calibrated well from patients with low, normal, and high ICP. The mean ± standard deviation (SD) for the sum of squared errors (SSE) and R^2 for all patients was 4.02 ± 2.11 mmHg and 0.92 ± 0.04, respectively.

Table 1
Mean ± SD for the values of the optimal parameters for all patients and the optimal parameter values for Patient 1.

Parameters	Mean ± SD	Patient 1	Units
P_{a0}	4.06 ± 2.36	6.96	mmHg
P_{v0}	5.68 ± 1.65	3.78	mmHg
P_{c0}	8.92 ± 3.19	10.30	mmHg
P_{s0}	4.13 ± 1.98	3.82	mmHg
K_a	0.77 ± 0.56	0.58	ml^{-1}
K_v	2.15 ± 0.30	1.87	ml^{-1}
K_c	2.43 ± 0.63	2.23	ml^{-1}
K_s	1.83 ± 0.52	1.50	ml^{-1}
P_e	6.64 ± 3.44	5.55	mmHg
P_t	6.03 ± 4.47	4.39	mmHg
$P_{s,out}$	7.22 ± 5.33	4.82	mmHg
L_e	0.06 ± 0.04	0.04	mmHg s^2/ml
L_s	0.09 ± 0.06	0.04	mmHg s^2/ml
B_e	0.0178 ± 0.0113	0.0025	mmHg s^2/ml^2
B_s	0.11 ± 0.04	0.16	mmHg s^2/ml^2
B_v	0.16 ± 0.09	0.06	mmHg s^2/ml^2

Fig. 3 presents the model curves for CSF flow and venous outflow for two patients, Patient 1 and 10. We observed that the model behaves as in data for the venous outflow. For the CSF flow, we saw a slightly higher peak flow, a fast decrease in flow after the peak, and some oscillation of flow towards the end of the period.

The model curves for volume changes, pressure changes, and flow in and between the compartments for all patients are given in Supplementary B. The mean and SD of optimal parameter values for all patients and the individual parameter values for Patient 1 are given in Table 1 and the individual parameter values for all patients are given in Supplementary A. Patient 1 was chosen as ICP was within normal in range and profile.

Using the optimal parameter values for Patient 1, we simulated the model to picture different intracranial dynamics. Fig. 4 shows the temporal evolution of ICP, arterial inflow, venous outflow, CSF flow, slight compression of the brain tissue, and venous collapse in one

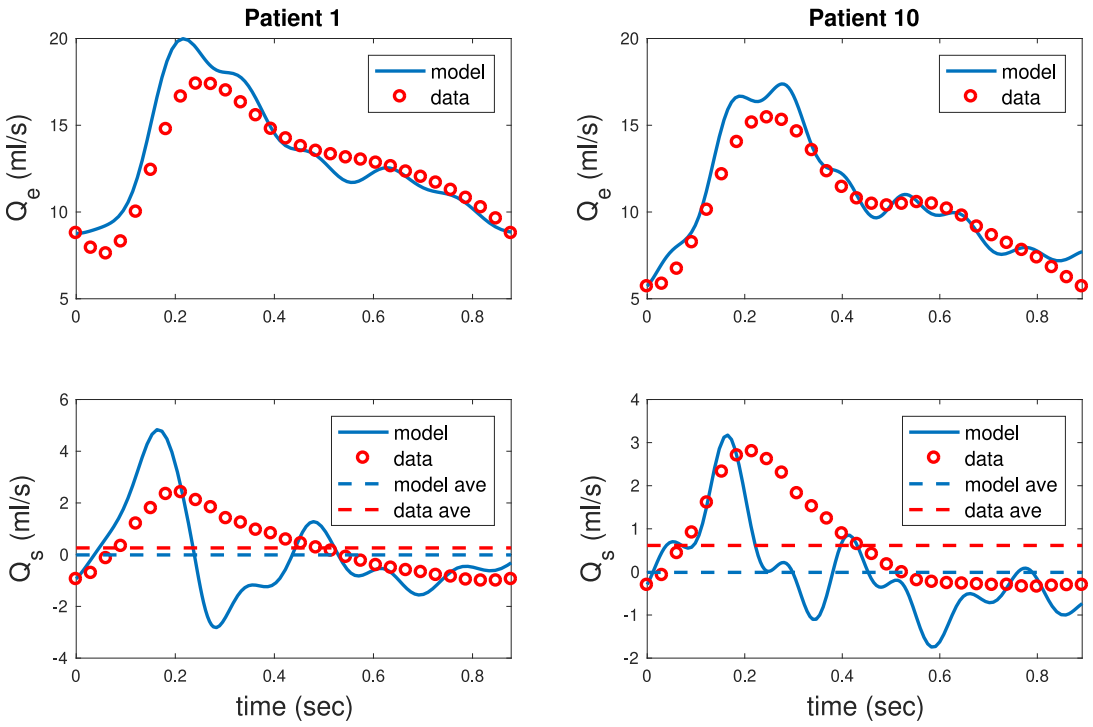

Fig. 3. The venous outflow (Q_e) curves and CSF flow (Q_s) curves for two patients. The blue lines are the curves from the model and the red circles are data. For Q_e, the value of R^2 were 0.75 and 0.85 for Patient 1 and 10, respectively. For Q_s, the value of R^2 was low and the average of the data gave a better fit. We note that CSF flow measurements were subject to relatively large uncertainties. Also, flow data were average values over 2 min (around 120 heart cycles), hence, they appeared smoother than flow over one heart cycle. Nevertheless, average CSF flow from model and data were close and model CSF flow were within a physiologically acceptable range.

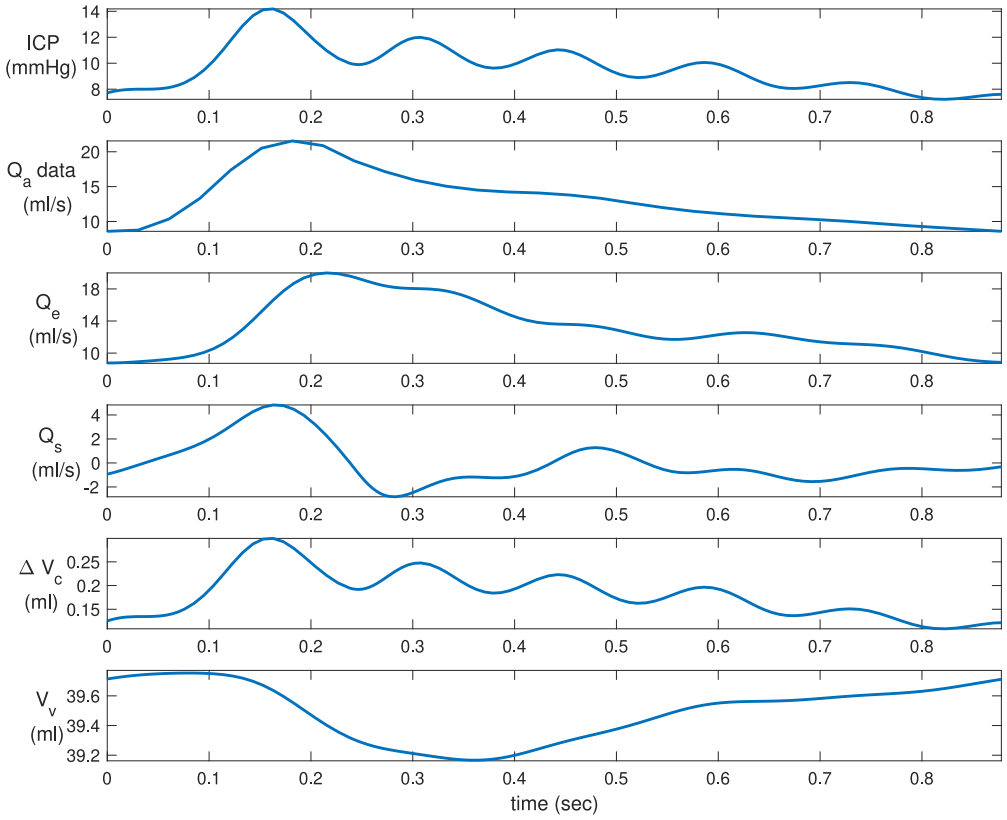

Fig. 4. Temporal plots of ICP, arterial inflow (Q_a), venous outflow (Q_e), CSF flow (Q_s), slight compression of the brain tissue ($-\Delta V_c$), and venous collapse (V_v) over one period.

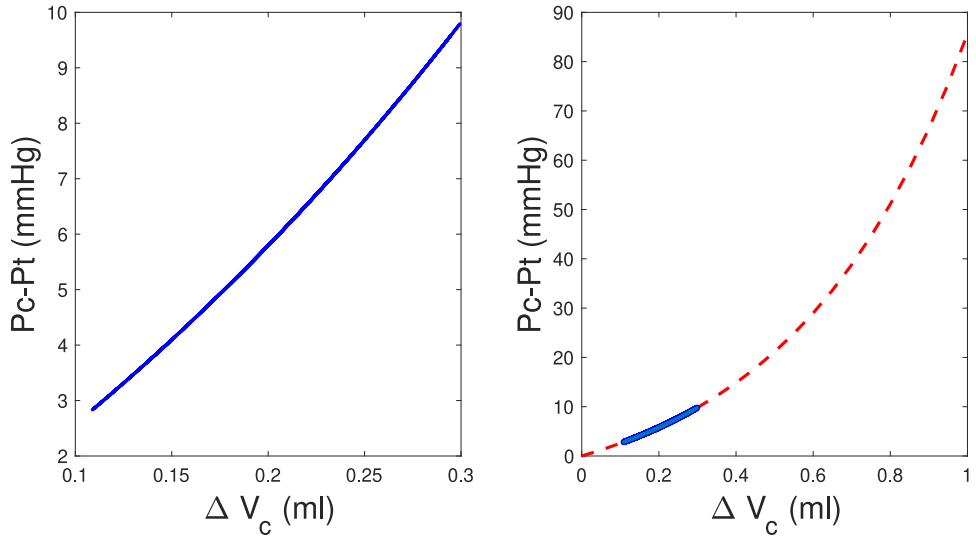

Fig. 5. (Left:) Pressure–volume curve in the intracranial compartment for low pressure and addition of small volumes, where the curve was fairly linear. (Right:) Pressure–volume curve in the intracranial compartment, which was projected for up to 1 ml change in stressed volume to show exponential nature.

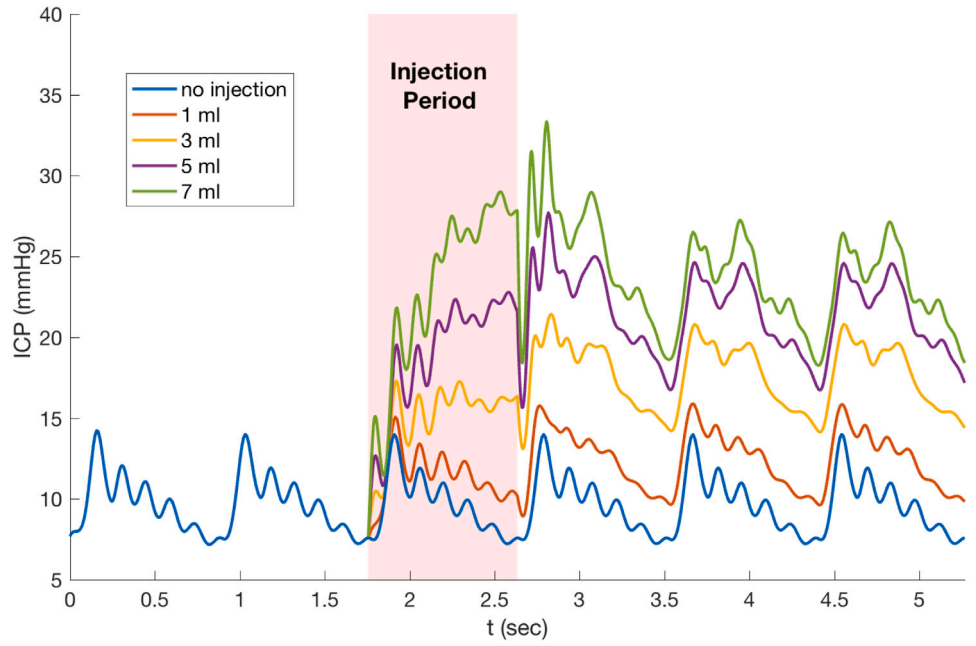

Fig. 6. The ICP response curves in relation to introduction of fluid with volume 1, 3, 5, and 7 ml into the intracranial compartment. The introduction/injection was given at a rate of $1/T$, $3/T$, $5/T$, and $7/T$, respectively, for one heart cycle (third period).

period. Fig. 5 presents the pressure–volume curve in the intracranial compartment.

In Fig. 6, the ICP response to an addition of fluid volume equal to 1, 3, 5, and 7 ml to the intracranial compartment are presented. The introduction/injection was given at a rate of $1/T$, $3/T$, $5/T$, and $7/T$, respectively, for one heart cycle.

In Fig. 7, the withdrawal of CSF volume equal to 1, 2, 3, and 4 ml from the intracranial compartment is simulated. The withdrawal rate, Q_l, was $-1/T$, $-2/T$, $-3/T$, and $-4/T$ ml/s for one period.

We simulated the ICP response when CSF was not absorbed into the venous system. In particular, Fig. 8 (Left) shows the effect of a continuous accumulation of CSF, $Q_l = 0.35$ ml/min, around 10, 20, and 30 min after it started. Furthermore, the ICP response to a CSF leak out of the cranium greater than its production was simulated. Fig. 8 (Right) presents the effect of a continuous leak of CSF, $Q_l = -0.06$ ml/min, around 10, 20, and 30 min after it started.

3.2. Sensitivity

In this section, we examined different parameter variation and the resulting effect on the model ICP. Here, we took note of the model parameters that affect the ordering of ICP curve peaks according to height and the frequency of ICP curve oscillations. We did this by observing the changes in the ICP curve (over one period) when we varied a given parameter from a 95% reduction of its optimal value to a 95% increase of its optimal value for Patient 1 (see Table 1). We note that Patient 1 had a normal range of ICP values and profile. We observed the effects of the variation at the fifth cycle of the ICP curve where it had already attained a periodic behavior. The two-dimensional and three-dimensional sensitivity plots for ICP on variations of all the optimized model parameters are given in Supplementary C and Supplementary D, respectively.

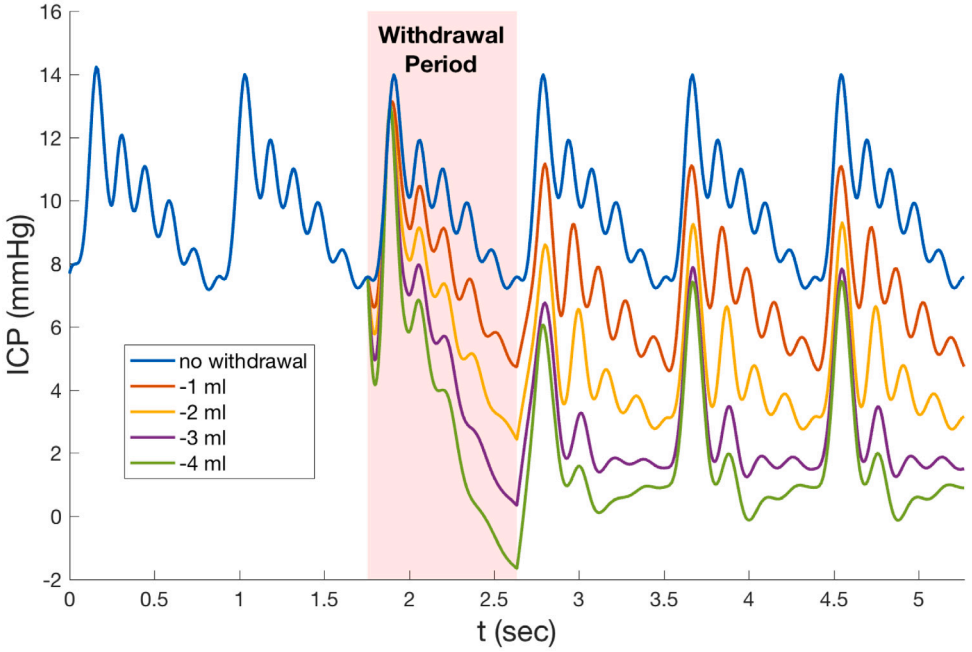

Fig. 7. The ICP response curves in relation to withdrawal of fluid of volume −1, −2, −3, and −4 ml from the intracranial compartment. The withdrawal rate was −1/T, −2/T, −3/T, and −4/T ml/s for one heart cycle (third period).

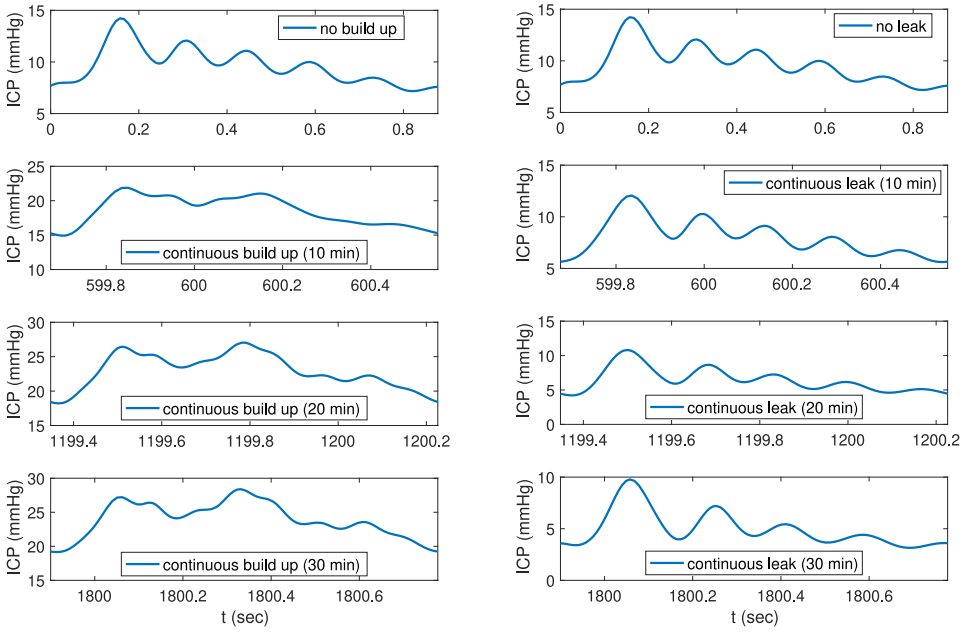

Fig. 8. (Left) The ICP response curves in relation to continuous build up of CSF (Q_l = 0.35 ml/min) into the cranial compartment at 10, 20, and 30 min after the start of the accumulation. (Right) The ICP response curves in relation to continuous leak (Q_l = −0.06 ml/min) out of the cranial compartment at 10, 20, and 30 min after the start of the leak.

We found that a large decrease in P_{a0} or K_a, a large increase in P_{v0} or K_v, a decrease in B_s, or a large increase in B_v influenced the order of the peaks in terms of height. We illustrate these in Fig. 9.

We observed that the change in frequency of oscillations in the ICP was due to change in wavelength or due to merging of waves. The change in frequency of oscillations due to change in wavelength was most notable in a directly proportional change in P_{c0} or K_c. Small changes in wavelength could also be observed with a change in P_{v0}, K_v, P_t, or B_s. As an illustration, we show the sensitivity plots for K_c and P_t in Fig. 10. The decrease in frequency due to merging of waves could be observed for large increase P_{s0}, K_s, or B_v, increase in P_e, or decrease in $P_{s,out}$, L_s, or L_e. As an illustration, we show the sensitivity plots for K_s and L_e in Fig. 11.

3.3. ICP curve categorization

In this section, we categorized two-parameter changes in accordance to how they affect the order in terms of height of the 3 main peaks of the ICP curve. Theoretically, we have 6 configurations: P123, P132, P213, P231, P321, and P312. In the notation, the first number after 'P' denotes the highest peak, followed by the next number, then the last number being the lowest peak. For example, P312 means that

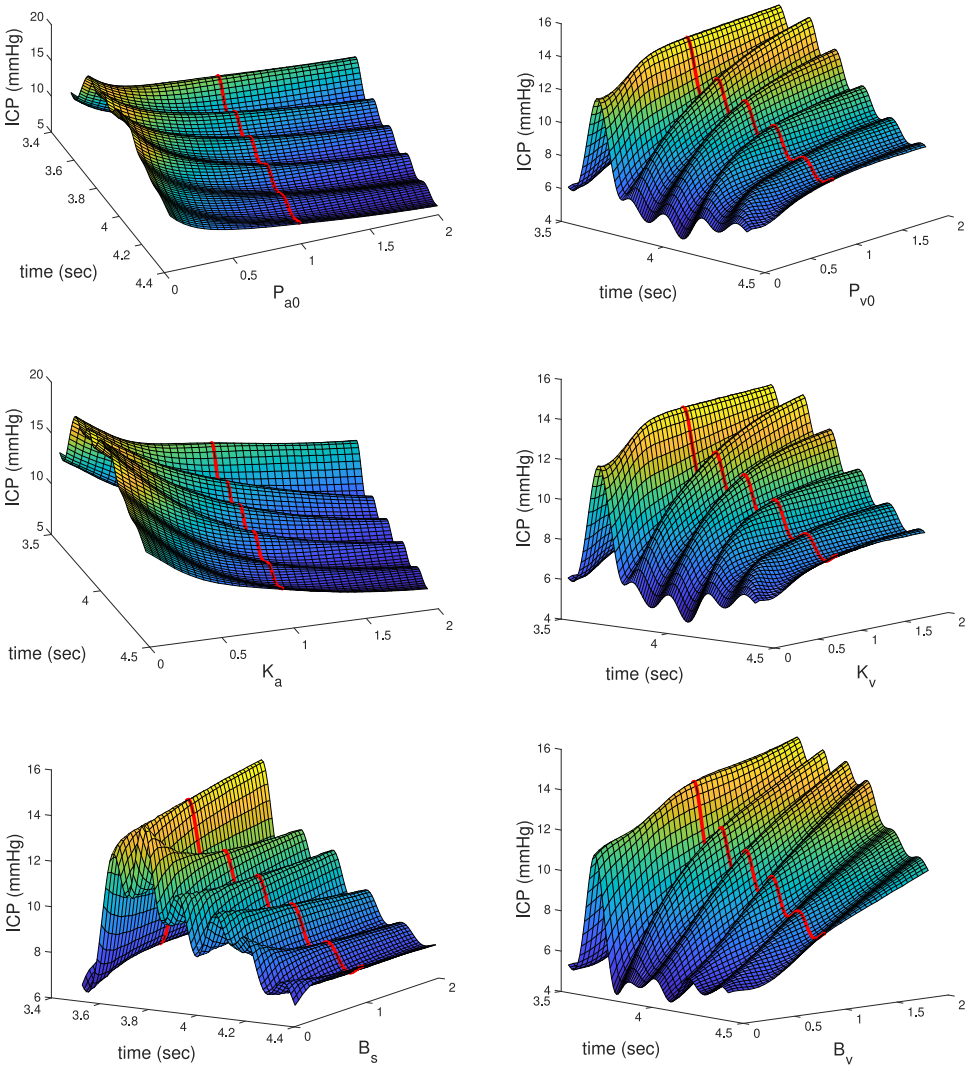

Fig. 9. Sensitivity plot for ICP on variations in P_{a0}, P_{v0}, K_a, K_v, B_s, and B_v where the parameters were varied from a 95% reduction of their optimal value up to a 95% increase. The red curve corresponds to the ICP at their respective optimal values.

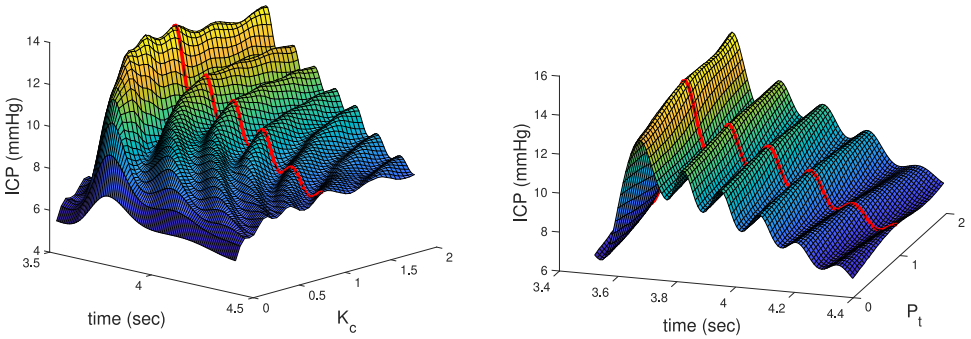

Fig. 10. Sensitivity plot for ICP on variations in K_c and P_t where the parameters were varied from a 95% reduction of their optimal value up to a 95% increase of their optimal value. The red curve corresponds to the ICP at their respective optimal values.

the third peak is the highest followed by the first peak then the second peak. Furthermore, there was the case of merging among the 3 main peaks, which may lead to only 2 main peaks or one. We denote P21 and P12 for two peaks and P1 for one.

From the sensitivity analysis, we saw that the parameters affecting the order of the dominant peaks were mainly P_{a0}, K_a, P_{v0}, K_v, B_s, and B_v. We varied these parameters two at a time and observed their effect on the order of the peaks. In Fig. 12, we present the classification of the order of the peaks relative to changing the elastance parameters in the arterial and venous compartment. We saw 4 qualitative classes for the change in arterial elastance parameters while we saw 2 for the change in venous elastance parameters. When arterial elastance parameters

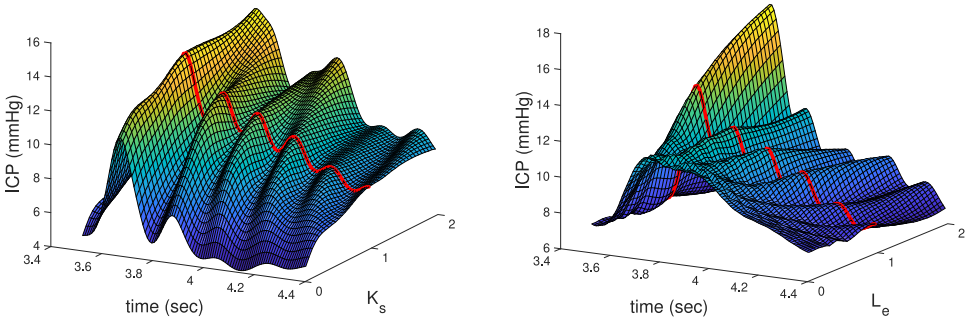

Fig. 11. Sensitivity plot for ICP on variations in K_s and L_e where the parameters were varied from a 95% reduction of their optimal value up to a 95% increase of their optimal value. The red curve corresponds to the ICP at their respective optimal values.

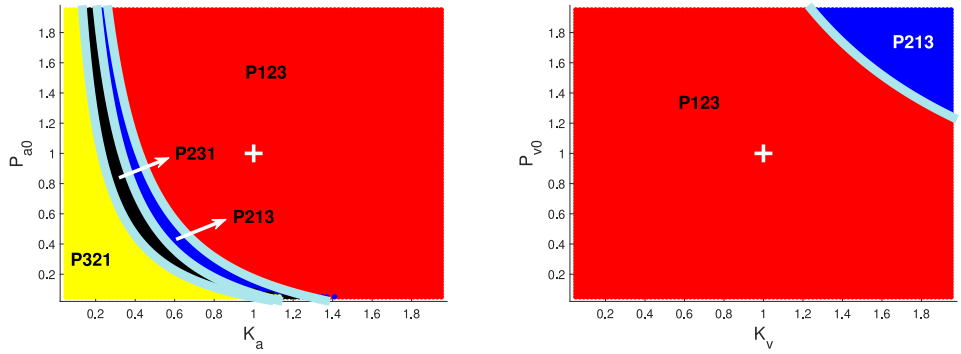

Fig. 12. Color map representation of the change in order of the peaks as the elastance parameters in the arterial compartment (left panel) and venous compartment (right panel) were changed. The color red corresponds to P123, blue to P213, black to P231, and yellow to P321. The boundaries can be approximated by curves of the form $y = ax^b + c$. The values for a, b, and c for the boundary curves are given in Supplementary E.

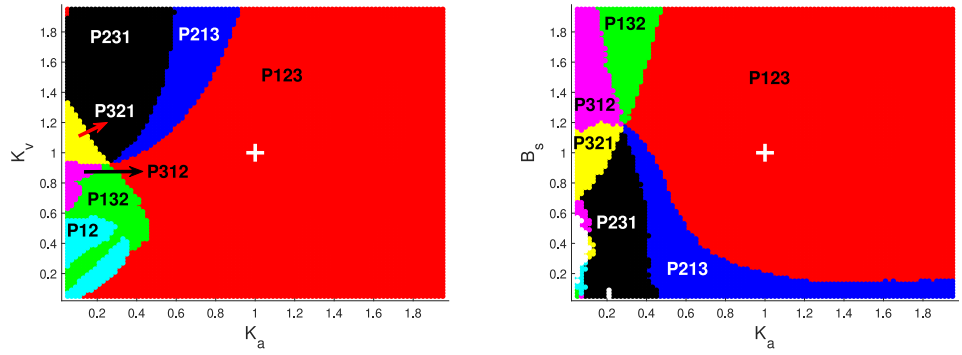

Fig. 13. Color map representation of the change in order of the peaks for K_a vs K_v (left panel) and K_a vs B_s (right panel). The color red corresponds to P123, blue to P213, green to P132, black to P231, yellow to P321, magenta to 312, white to P21, and cyan to P12.

were decreased, pathological peak patterns appeared while an increase in venous elastance parameters led to a potentially pathological peak pattern. In Fig. 13, we present the classes when we changed elastance parameters in the arterial and venous compartments at the same time. In this case, we observed more classes of peak patterns. We saw that a 70% decline in K_a transformed the state into a highly sensitive region. The color maps for the effect of the variations in the other parameters are given in Supplementary E.

4. Discussion

Our current knowledge of human CBF was attained through studies using single measurements. From these studies we know that the normal brain adjusts blood flow to meet the metabolism (Lassen, 1959) a mechanism fairly independent of blood pressure variations (Meng and Gelb, 2015). These features are called metabolic coupling and cerebral autoregulation, feature securing optimal perfusion to the brain tissue, avoiding both edema and ischemia. In most acute brain catastrophes, the metabolic coupling and/or cerebral autoregulation are malfunctioning making it vital for the treating physician to optimize CBF under these pathologic situations. Such patients are routinely monitored with online ICP. The ICP curve is a constellation of intracranial arterial inflow and the compensatory venous and CSF reaction. Theoretically a mathematical model can describe this interplay and the ICP curve form can then provide information about the intracranial arterial, venous and CSF system status, vital information to the treating physician in order to optimize the handling of each single patient.

A mechanism-based model of ICP was proposed and calibrated to data. We have shown that a simple CBF model was able to capture the complex dynamics of blood flow, CSF flow, volume changes, and pressure changes in the intracranial cavity. Through the model, we were able to present the dynamics of CBF over the course of one

heart cycle. A sensitivity analysis on the changes in ICP provided a deeper understanding and classification of the ICP curve morphology in terms of parameter changes. The model also presents a quantification of intracranial compliance and the ability to simulate leak/accumulation of fluid in the intracranial cavity.

4.1. Model development

We utilized stressed volume in the compartments and flow between compartments as state variables. In the original mathematical model on human intracranial hydrodynamics by Ursino (1988), the system differential equations were in terms of change in pressure, dP/dt. This was also the case in Olufsen et al. (2005), presenting a compartmental model involving CBF. The expression for dP/dt was obtained from taking the derivative of the linear relation of volume and pressure, $V = cP$, where c is compliance. The derivative being

$$\frac{dV}{dt} = c\frac{dP}{dt} + P\frac{dc}{dt} = Q_{in} - Q_{out}. \tag{22}$$

For models involving non-constant or state-dependent compliance, as in the case of our model, taking the rate of change of compliance adds more complexity. However, using volume in the compartments as state variables is a simpler alternative (Domogo and Ottesen, 2021). Moreover, using stressed volume instead; we further simplified the system by having less parameters to optimize. This comes with the simplification that unstressed volumes in the compartments were assumed constant. Since our focus was the dynamics in a period of one heart cycle this was reasonable. With these, we were able to incorporate a state dependent compliance, inherent to the model, without having to deal with its derivative. State dependent compliance was used in former ICP models in Marmarou et al. (1978), Unnerbäck et al. (2020), Ursino (1988) but a constant compliance (Olufsen et al., 2005) was a simplification. To the best of our knowledge, there is no CBF model involving state dependent compliance inherent from a general mono-exponential pressure–volume relation in the arterial, intracranial, and spinal compartments and pressure–volume relation as in collapsible tubes in the venous compartment. In relation to flow, the use of the unsteady Bernoulli equation was advantageous because of 3 features. First, it involves inertance. This brings about delay in the hydrodynamic effects of pressure changes within the intracranial compartments, which may cause oscillations in the ICP curve (Unnerbäck et al., 2020). Indeed, we observed from the sensitivity analysis in Section 3.2 that letting the venous outflow inertance go to zero leads to the loss of oscillations (see Fig. 11). Second, it incorporates a state dependent resistance. A large change in arterial pressure does not change CBF (Guyton and Hall, 2016). In our model, this was captured by the resistance itself being proportional to the flow. Finally, it captured the two-directional flow between the intracranial cavity and the spine through the foramen magnum.

4.2. ICP curve morphology

The physiological causes of the ICP curve morphology have been a continuing discussion for years (Balédent et al., 2018). Earlier studies have been looking at the relation of ICP and the intracranial arterial blood pressure (Unnerbäck et al., 2020). Recently, studies pointed to the dynamics of blood flow and CSF flow as an explanation of the ICP curve morphology (Alperin et al., 2000; Unnerbäck et al., 2018). In particular, the peaks may be the product of the natural physiological properties in the intracranial cavity that depend on intracranial arterial blood inflow and intracranial compensatory mechanisms (Unnerbäck et al., 2020). In general, the shape of the ICP curve was shown to be the result of dynamics between arterial, venous, and CSF flow compensated by elasticity of the intracranial cavity (Nornes et al., 1977; Avezaat and van Eijndhoven, 1986; Balédent et al., 2006).

Our model was able to capture the interaction of blood flow and CSF flow moderated by compliance of the intracranial cavity. Moreover, the model gave a visualization of these dynamics through the course of one heart cycle. In Fig. 4, we observed that surge in arterial inflow is in conjunction with ICP increase that oscillates back to its original value. The rapid arterial inflow was compensated by increase in venous outflow, increase in CSF flow, and a slight compression of the brain tissue (Greitz et al., 1992; Unnerbäck et al., 2020). Note that the small volume oscillations in V_c compress the brain tissue, V_t, only insignificantly. We noticed the collapse of the veins at increased ICP, which suggests that this is one way of compensatory behavior that helps increase venous outflow. Note that the collapse of the cerebral venous bed is influenced by ICP (Ursino, 1988). Now, one of the main role of the CSF is to cushion the brain within the hard skull (Guyton and Hall, 2016). In relation to this, we observed that after compression the brain tissue oscillates back to its original state. Notice that this is in conjunction with the oscillatory behavior of the CSF flow after reaching its climax. This oscillatory dampening of the decompression of the brain tissue may be attributed to the cushioning effect of CSF.

Furthermore, we uncovered the parameters that predominantly affect ICP morphology. From the sensitivity analysis in Section 3.2, we identified the order in terms of height of the 3 main peaks of the ICP curve, which was affected by a sufficient decrease in arterial elastance, a sufficient large increase in resistance to arteriovenous flow, a sufficient large increase in venous elastance, or a sufficient decrease in resistance to CSF flow in the foramen magnum. Frequency of oscillations in the ICP curve was most sensitive to change in intracranial elastance.

Finally, we classified the order of the peaks according to two parameters simultaneously varied. Note that the ICP curve over one heart cycle is formed by 3 main peaks, denoted as P1, P2, and P3 (Carrera et al., 2010). Also, the shape of the ICP is used to guide management of brain diseases. In Nucci et al. (2016), they have identified normal, potentially pathological, likely pathological, pathological cases based on the arrangement of the 3 main peaks of ICP. In Section 3.3, we provided a visual classification of the different order of the 3 main peaks of the ICP curve. We showed the evolution of the peaks brought about by simultaneous changes in two parameters and classified which configuration occur with these parameter changes. We observed that the changes in order of the 3 main peaks were mainly influenced by a decrease in arterial elastance. At decreased arterial elastance, small perturbation in venous elastance, CSF flow resistance, or arteriovenous flow resistance led to different configurations.

4.3. Intracranial compliance

What is intracranial compliance really? Theoretically, it is a function relating change in ICP to a change in corresponding volume of the intracranial contents. The Monro-Kellie doctrine (Czosnyka and Citerio, 2012) states that the sum of intracranial volumes, brain tissue, CSF, arterial and venous blood, is constant. The intracranial compliance concept is particularly complex as an increase in one of the above mentioned volumes should cause a compensatory reciprocal decrease in either one or both of the remaining where each volume have its own specific in- and outflow pattern. Different methods have been presented in order to assess intracranial compliance (Szewczykowski et al., 1977; Cardoso et al., 1983; Robertson et al., 1989; Czosnyka et al., 1996, 1997). None of these methods directly describe intracranial compliance fully. Thus, using them to deduce changes in brain compliance must be done with utmost care (Czosnyka and Citerio, 2012).

Through the compartmentalization of the intracranial cavity introduced in Unnerbäck et al. (2020) and adapted in our model, we were able to quantify the change in volume and change in pressure of the compartment containing the arterial, venous, and CSF compartments. In our model, we denoted it as the intracranial compartment. We used a mono-exponential function to represent the pressure and volume relationship in this compartment as suggested in Marmarou et al. (1978), Avezaat et al. (1979) and used in Ursino (1988). Thus, the

compliance of this compartment is nonconstant. In Eq. (14), we see that the compliance of the intracranial compartment is an exponential decaying function of stressed volume. That is, the intracranial compartment becomes more noncompliant as stressed volume increases. In Fig. 5, we observed that the pressure–volume curve in intracranial compartment is almost linear in the normal range. This means that a constant compliance maybe a good approximation. This is in agreement with observations that the increase in intracranial elastance in man is fairly linear up to 30mmHg but afterward the increase becomes steeper (Friden and Ekstedt, 1983). Hence, considering brain diseases, e.g. causing edema, in the cranium, a constant compliance may not be suitable.

In clinical practice, compliance can be measured by withdrawal of a fixed CSF volume from the intracranial cavity and observing the change in diastolic ICP before and after withdrawal. Through the model, this compliance measurement could also be obtained. In Fig. 7 for example, we can divide the volume of fluid taken out of the intracranial compartment by the change in diastolic ICP before and after withdrawal.

4.4. ICP response simulations

We simulated the effect of addition or leak of fluid in the intracranial compartment Vc. Experimentally, this is done by fluid injection or removal of CSF, which are invasive maneuvers. This can be performed in neurological practice to gain information on intracranial dynamics and determine the value of physiologically important parameters like intracranial compliance and CSF outflow resistance [Ursino (1988)]. Through our model, we simulated these invasive operations without any risk to human safety. Specifically, we simulated the effect of cerebral edema, hydrocephalus, or intracranial hypotension on the ICP curve over one heart cycle. We note that simulations of infusion of artificial CSF into the intracranial compartment using a mathematical model were also done in Eklund et al. (2007).

In Fig. 6, the ICP response to an addition volume of 1, 3, 5, and 7 ml are observed. We observed that ICP attains a periodic behavior after 2 cycles and potentially pathological peak pattern appeared as greater volume of fluid was introduced, which were similarly observed in Eklund et al. (2007) during Bolus infusion. This simulation could be representative of an edema of size, e.g. 5 ml, which has formed in the period of 1 heart cycle.

In comparison to injection of fluid into the intracranial cavity, the extraction of fluid to determine intracranial elastance is a more common clinical practice. Both are invasive maneuvers but injection of fluid presents a greater threat to patient safety [Unnerbäck et al. (2019)]. In Fig. 7, we simulated the withdrawal of CSF volume equal to 1, 2, 3, and 4 ml and observed the same effect as in experiments.

The production of CSF is approximately 0.35 ml/min. In the event that these are not absorbed into the venous system then it will accumulate in the intracranial cavity, as in the case of hydrocephalus. In Fig. 8 (Left), we looked at the ICP response when CSF was not absorbed. We observed the increase in ICP and the formation of potentially pathological peak patterns as time went by, which is also similarly recorded during constant rate infusion of artificial CSF (Eklund et al., 2007; Andersson et al., 2011). On the other hand, intracranial hypotension is caused by a CSF leaking out of the cranium at a rate greater than its production. In Fig. 8 (Right), we observed the decrease in ICP and flattening of the ICP curve as CSF leaks out of the intracranial cavity.

4.5. Limitations

In this study, the optimized model parameter values were obtained through numerical methods. These optimal parameter values represent a local solution to the optimization problem, which may not be guaranteed to be within the physiological range. Also, it may be possible to find different sets of parameter values that provide similar model states (Pope et al., 2011). We addressed these considerations by deriving initial parameter values from related studies and patient-specific data. To a certain extent, this guaranteed that our local solution was near the true solution. Also, the model had been calibrated well with ICP data from 10 persons where obtained optimal values were within acceptable variation. Furthermore, the obtained venous outflow and CSF flow in the foramen magnum curves were within a physiologically accepted range. The deviation between venous outflow and CSF flow over time could be due to model simplification. Note that blood is a non-Newtonian fluid with rheological properties, so it is more viscous compared to Newtonian fluids. But in modeling studies, non-Newtonian rheology is seldom considered at the systemic level. Instead, blood is commonly described as a Newtonian fluid for less complexity (Domogo and Ottesen, 2021). Also, viscosity, which is not factored into the unsteady Bernoulli equation, affects CSF flow (Støverud et al., 2013). Although the Bernoulli equation may be sufficient to characterize CSF flow in persons without obstructed subarachnoid spaces, it was shown that for patients with obstruction it is more precise to use the Navier–Stokes equation (Støverud et al., 2013; Ringstad et al., 2017; Sartoretti et al., 2019). But, the deviations may also reflect measurement errors. Flow and ICP were measured in very small time intervals (of length around 30 ms). This may cause complications in calibrating time for the various measurements, which may lead to errors. The flow was calculated from CMRi scans over the period of 2 min (around 120 heart cycles) at homeostatic stable condition. From this, flow over 1 heart cycle is calculated, giving an average flow curve. Hence, a smoother curve is observed from data compared to model output. Note that CSF flow in the cerebral aqueduct is oscillatory, which is dependent on breathing and heart beat (Markenroth Bloch et al., 2018). Also, it may be the case that the small magnitudes of the CSF flow measurements are accompanied by relative large uncertainties (Unnerbäck et al., 2020). Furthermore, venous flow measured in the jugular veins, as in the case of data, is different from venous flow at the point of exit in the cranial cavity (Stoquart-Elsankari et al., 2009). Compared to most modeling using simple models of complex systems the validation of model generated CSF flow and venous outflow by experimentally obtained values is adequate in the sense that earlier studies are only able to perform validation with average values (Gadda et al., 2016). If we instead add more details in the model (which may be more speculative or less certain than desired) then more unknown parameters would be introduced. With more unknown parameters, we may achieve greater model accuracy but the reliability of the findings would decrease. For this study, we strike a balance between model accuracy and reliability but we recognize that further work is needed to understand the deviations.

In CBF modeling, autoregulation is a very important mechanism and it plays a crucial role over timespan longer than one heart beat. In the current paper, we study the faster oscillatory patterns during a single heart beat where autoregulation plays an insignificant role (Klein et al., 2019; Panerai, 2008). Hence, autoregulation is not incorporated in the model. In future work we expect to study the dynamics over several heart beats by extending the present model to incorporate autoregulation, among others. Moreover, the compliance of the intracranial compartment does not always change exponentially. It is linear for low pressures, then it becomes exponential for increased pressures, and it deflects to the right when ICP causes cerebral arterioles and arteries to collapse. However, for low pressures the exponential is well approximated by a linear relation and we are not in the range of extremely high pressures where deflection are seen, that is, we have arterial pressure that is always greater than ICP. Hence, the mono-exponential pressure–volume relation is a simple way of capturing the compliance of the intracranial compartment while unnecessarily introducing additional parameters and complexity in the model.

Another mechanism that is important over longer timespan is CSF production and absorption. In future work, where study the dynamics over several heart beats, we may add more details into the model by incorporating CSF production and absorption as given in Eklund et al. (2007). This may improve the deviations between CSF flow from the model and data.

5. Conclusion

In conclusion, we have developed a simple mechanistic and patient-specific compartmental model of CBF involving the cerebral arteries and veins, CSF, and the brain tissue. We were able to take into account different features of intracranial dynamics simultaneously. Specifically, we used a mono-exponential pressure–volume relationship in the intracranial compartments, pressure–volume relation in collapsible tubes in veins, and the unsteady Bernoulli equation to represent fluid flow. Through an iterated constrained-ODE optimization routine, the model was calibrated well with ICP data from 10 patients over the period of a heart cycle while at the same time providing venous outflow and CSF flow in the foramen magnum that were within acceptable physiological range. Moreover, we determined patient-specific model parameter values, e.g., physiologically important parameter values like intracranial compliance, arterial elastance, venous elastance, and venous outflow resistance. Through sensitivity analysis, we identified the parameters that affected the order of the 3 main peaks and frequency of oscillations in the ICP curve. In particular, decrease of arterial elastance or large increase in resistance to arteriovenous flow led to pathological peak patterns. Increase in venous elastance or large decrease in CSF flow resistance led to potentially pathological peak patterns. Furthermore, the compliance of the intracranial compartment had a notable effect on the frequency of oscillations in the ICP curve. We presented an alternative to invasive maneuvers used to measure ICP response to injection/removal of CSF through model simulations. In this illustration, ICP response over one heart cycle during the onset of brain edema, hydrocephalus, and intracranial hypotension was simulated. Through the mechanistic model, which could be calibrated to different patients, pathological peak patterns were clarified by the values of model physiological parameters or the accumulation/leak of fluid in the intracranial cavity. This presents an approach for medical doctors and the pharmaceutical industry to help them address the causes underlying patient-specific intracranial conditions instead of treating observed symptoms.

CRediT authorship contribution statement

Andrei A. Domogo: Conceptualization, Methodology, Software, Formal analysis, Investigation, Writing – original draft. **Peter Reinstrup:** Formal analysis, Investigation, Validation, Writing – review & editing, Supervision. **Johnny T. Ottesen:** Conceptualization, Methodology, Formal analysis, Validation, Writing – review & editing, Supervision.

Declaration of competing interest

The authors declare that they have no known competing financial interests or personal relationships that could have appeared to influence the work reported in this paper.

Acknowledgments

This study was made possible through the Alternate Study Grant of the University of the Philippines and support of Roskilde University, Denmark, University of the Philippines Baguio, and the Philippine Commission on Higher Education.

Appendix A. Supplementary data

Supplementary material related to this article can be found online at https://doi.org/10.1016/j.jtbi.2023.111451.

References

Alperin, N., Lee, S., Loth, F., Raksin, P., Lichtor, T., 2000. MR-intracranial pressure (ICP) a method to measure intracranial elastance and pressure noninvasively by means of MR imaging: baboon and human study. Radiology 217, 877–885.

Alperin, N., Lee, S., Sivaramakrishnan, A., Hushek, S., 2005. Quantifying the effect of posture on intracranial physiology in humans by MRI flow studies. J. Magn. Reson. Imaging 22, 591–596.

Andersson, K., Sundström, N., Malm, J., Eklund, A., 2011. Effect of resting pressure on the estimate of cerebrospinal fluid outflow conductance. Fluids Barriers CNS 8, 15.

Avezaat, C., Eijndhoven, J.V., Wyper, D., 1979. Cerebrospinal fluid pulse pressure and intracranial volume-pressure relationship. J. Neurol. Neurosurg. Psychiatry 42, 687–700.

Avezaat, C., van Eijndhoven, J., 1986. The role of the pulsating pressure variations in intracranial pressure monitoring. Neurosurg. Rev. 9, 113–120.

Balédent, O., Czosnyka, M., Czosnyka, Z., 2018. Brain pulsations enlightened. Acta Neurochir. 160, 225–227.

Balédent, O., Fin, L., Khuoy, L., Ambarki, K., Gauvin, A., Gondry-Jouet, C., Meyer, M., 2006. Brain hydrodynamics study by phase-contrast magnetic resonance imagin and transcranial color Doppler. J. Magn. Reson. Imaging 24, 995–1004.

Balédent, O., Henry-Fuegas, M., Idy-Peretti, I., 2001. Cerebrospinal fluid dynamics and relation with blood flow: a magnetic resonance study with semiautomated cerebrospinal fluid segmentation. Invest. Radiol. 36, 368–377.

Bergel, D., 1961. The statis elastic properties of the arterial wall. J. Physiol. 156, 458–469.

Cardoso, E., Rowan, J., Galbraith, S., 1983. Analysis of the cerebrospinal fluid pulse wave in intracranial pressure. J. Neurosurg. 59, 817–821.

Carrera, E., Kim, D., Castellani, G., Zweifel, C., Czosnyka, Z., Kasparowicz, M., Smielewski, P., Pickard, J., Czosnyka, M., 2010. What shapes pulse amplitude of intracranial pressure? J. Neurotrauma 27 (2), 317–324.

Czosnyka, M., Batorski, L., Laniewski, W., Maksymowicz, W., Koszewski, W., Zaworski, W., 1990. A computer system for the identification of the cerebrospinal compensatory model. Acta Neurochir. (Wien) 105, 112–116.

Czosnyka, M., Citerio, G., 2012. Brain compliance: the old story with a new 'et cetera'. Intensive Care Med. 38, 925–927.

Czosnyka, M., Guazzo, E., Whitehouse, M., Smielewski, P., Czosnyka, Z., Kirkpatrick, P., Piechnik, S., Pickard, J., 1996. Significance of intracranial pressure waveform analysis after head injury. Acta Neurochir. 138, 531–542.

Czosnyka, M., Piechnik, S., Richards, H., Kirkpatrick, P., Smielewski, P., Pickard, J., 1997. Contribution of mathematical modelling to the interpretation of bedside tests of cerebrovascular autoregulation. J. Neurol. Neurosurg. Psychiatry 63, 721–731.

Daouk, J., Bouzerar, R., Baledent, O., 2016. Heart rate and respiration influence on macroscopic blood and CSF flows. Acta Radiol. 1–6.

Domogo, A., Ottesen, J., 2021. Patient-specific parameter estimation: coupling a heart model and experimental data. J. Theoret. Biol. 526.

Eide, P., Brean, A., 2006. Intracranial pulse pressure amplitude levels determined during preoperative assessment of subjects with possible idiopathic normal pressure hydrocephalus. Acta Neurochir. (Wien) 148, 1151–1156.

Eklund, A., Smielewski, P., Chambers, I., Alperin, N., Malm, J., Czosnyka, M., Marmarou, A., 2007. Assessment of cerebrospinal fluid outflow resistance. Med. Biol. Eng. Comput. 45, 719–735.

Ellwein, L., Tran, H., Zapata, C., Novak, V., Olufsen, M., 2008. Sensitivity analysis and model assessment: Mathematical models for arterial blood flow and blood pressure. Cardiovasc. Eng. 8, 94–108.

Friden, H., Ekstedt, J., 1983. The CSF volume-pressure relationship in man. In: Ishii, S., Nagai, H., Brock, M. (Eds.), Intracranial Pressure V. Springer-Verlag, Hiedelberg: Berlin, pp. 252–260.

Gadda, G., Taibi, A., Sisini, F., Gambaccini, M., Sethi, S., Utriainen, D., Haacke, E., Zamboni, P., Ursino, M., 2016. Validation of hemodynamic model for the study of the cerebral venous outflow system using MR imaging and echo-color Doppler data. AJNR Am. J. Neuroradiol. 37 (11), 2100–2109.

Greitz, D., Wirenstam, R., Frank, A., Nordell, B., 1992. Pulsatile brain movement and associated hydrodynamics studied by magnetic resonance phase imaging. Neuroradiology 34, 370–380.

Grimes, R., Levine, R., Walker, P., Yoganathan, A., 1995. Dynamics of systolic pulmonary venous flow in mitral regurgitation: Mathematical modeling of the pulmonary venous system and atrium. J. Am. Soc. Echocardiogr. 8, 631–642.

Guillaume, J., Janny, P., 1951. Manometrie intra-cranienne continue; Interet de la methode et premiers resultats. Rev. Neurol. Psychiatr. 84, 131.

Guyton, A., Hall, J., 2016. Textbook of Medical Physiology, thirteenth ed. Elsevier Inc.

Hayashi, K., Handa, H., Nagasawa, S., Okumura, A., Moritake, K., 1980. Stiffness and elastic behavior of human intracranial and extracranial arteries. J. Biomech. 13, 175–184.

Hu, X., Glenn, T., Scalzo, F., Bergsneider, M., Sarkiss, C., Martin, N., Vespa, P., 2010. Index of cerebrospinal compensatory reserve in hydrocephalus. Physiol. Meas. 5 (31), 679–695.

Hua, J., Liu, P., Donahue, M., Rane, S., Chen, J., Qin, Q., Kim, S., 2019. MRI techniques to measure arterial and venous cerebral blood volume. NeuroImage 187, 17–31.

Kim, D., Czosnyka, Z., Keong, N., Radolovich, D., Smielewski, P., Sutcliffe, M., Pickard, J., 2009. Index of cerebrospinal compensatory reserve in hydrocephalus. Neurosurgery 64, 494–502.
Klein, S., Depreitere, B., Meyfroidt, G., 2019. How I monitor cerebral autoregulation. Crit. Care 23, 160.
Lassen, N., 1959. Cerebral blood flow and oxygen consumption in man. Phys. Rev. 39, 183.
Lundberg, N., 1960. Continuous recording and control of ventricular fluid pressure in neurosurgical practice. Acta. Psychiatr. Scand. Suppl. 36, 1–193.
Markenroth Bloch, K., Töger, J., Ståhlberg, F., 2018. Investigation of cerebrospinal fluid flow in the cerebral aqueduct using high-resolution phase contrast measurements at 7T MRI. Acta Radiol. 59 (8), 988–996.
Marmarou, A., Shulman, K., Rosende, R., 1978. A nonlinear analysis of the cerebrospinal fluid system and intracranial pressure dynamics. J. Neurosurg. 48, 332–344.
McArdle, W., Katch, F., Katch, V., 2006. Exercise Physiology, seventh ed. Lippincot, Williams & Wilkins, Baltimore.
Meng, L., Gelb, A., 2015. Regulation of cerebral autoregulation by carbon dioxide. Anesthesiology 122, 196–205.
Nornes, H., Aslid, R., Lindegaard, K., 1977. Intracranial pulse pressure dynamics in patients with intracranial hypertension. Acta Neurochir. 38, 177–186.
Nucci, C., Bonis, P.D., Mangiola, A., Santini, P., Sciandrone, M., Risi, A., Anile, C., 2016. Intracranial pressure wave morphological classification: automated analysis and clinical validation. Acta Neurochir. 158, 581–588.
Olufsen, M., Ottesen, J., Tran, H., Ellwein, L., Lipsitz, L., Novak, V., 2005. Blood pressure and blood flow variation during postural change from sitting to standing: model development and validation. J. Appl. Physiol. 99, 1523–1537.
Panerai, R., 2008. Cerebral autoregulation: From models to clinical applications. Cardiovasc. Eng. 8, 42–59.
Pope, S., Ellwein, L., Zapata, C., Novak, V., Kelly, C., Olufsen, M., 2011. Estimation and identification of parameters in a lumped cerebrovascular model. Math. Biosci. Eng. 6 (1), 93–115.
Rideout, V., 1991. Mathematical and Computer Modeling of Physiological Systems. Prentice Hall, Englewood Cliffs.
Ringstad, G., Lindstrøm, E., Vatnehol, S., Mardal, K., Emblem, K., Eide, P., 2017. Non-invasive assessment of pulsatile intracranial pressure with phase-constrast magnetic resonance imaging. PLoS One 12 (11), e0188896.
Robertson, C., Narayan, R., Contant, C., Grossman, R., Gokaslan, Z., Pahwa, R., Caram, Jr., P., Bray, Jr., R., Sherwood, A., 1989. Clinical experience with a continuous monitor of intracranial compliance. J. Neurosurg. 71, 673–680.
Sartoretti, T., Wyss, M., Sartoretti, E., Reischauer, C., Hainc, N., Graf, N., Binkert, C., Najafi, A., Sartoretti-Schefer, S., 2019. Sex and age dependencies of aqueductal cerebrospinal fluid dynamics parameters in healthy subjects. Front. Aging Neurosci. 11, 199.
Stoquart-ElSankari, S., Lehmann, P., Vilette, A., Czosnyka, M., Meyer, M., Deramond, H., Balédent, O., 2009. A phase-contrast MRI study of physiological cerebral venous flow. J. Cereb. Blood Flow Metab. 29, 1208–1215.
Stoquart-Elsankari, S., Lehmann, P., Vilette, A., Czosnyka, M., Meyer, M., Deramond, H., Balédent, O., 2009. A phase-contrast MRI study of physiological cerebral venous flow. J. Cereb. Blood Flow Metab. 29, 1208–1215.
Støverud, K., Langtangen, H., Haughton, V., Mardal, K., 2013. CSF pressure and velocity in obstructions of the subarachnoid spaces. J. Neuroradiol. 26, 218–226.
Szewczykowski, J., Sliwka, S., Kunicki, A., Dytko, P., Dip, P., Korsak-Sliwka, J., 1977. A fast method of estimating the elastance of the intracranial system. J. Neurosurg. 47, 19–26.
The Mathworks Inc., 2021 URL: https://www.mathworks.com/help/index.html.
Unnerbäck, M., Ottesen, J., Reinstrup, P., 2018. ICP curve morphology and intracranial flow-volume changes: a simultaneous ICP and cine phase contrast MRI study in humans. Acta Neurochir. 160, 219–224.
Unnerbäck, M., Ottesen, J., Reinstrup, P., 2020. Validation of a mathematical model for understanding intracranial pressure curve morphology. J. Clin. Monit. Comput. 34, 469–481.
Ursino, M., 1988. A mathematical study of human intracranial hydrodynamics part 1 - the cerebrospinal fluid pulse pressure. Ann. Biomed. Eng. 16, 379–401.
Westerhof, N., Stergiopulos, N., Noble, M., 2005. Snapshots of Hemodynamics, online ed. Springer US.